



# Ultra-high voltage efficiency rechargeable zinc-air battery based on high-performance structurally regulated metal-rich nickel phosphides and carbon hybrids bifunctional electrocatalysts

Yongxia Wang <sup>a</sup>, Jiaxi Liu <sup>a</sup>, Tuo Lu <sup>a</sup>, Rui He <sup>a</sup>, Nengneng Xu <sup>a</sup>, Jinli Qiao <sup>a,b,\*</sup>

<sup>a</sup> State Key Laboratory for Modification of Chemical Fibers and Polymer Materials, College of Environmental Science and Engineering, Donghua University, 2999 Ren'min North Road, Shanghai 201620, China

<sup>b</sup> Shanghai Institute of Pollution Control and Ecological Security, 1515 North Zhongshan Road, Shanghai 200092, China



## ARTICLE INFO

### Keywords:

Metal phosphides  
Porous carbon  
Oxygen reduction  
Oxygen evolution  
Zn-air battery

## ABSTRACT

Metal phosphides featuring electronic structure similar to Pt-group metal have triggered substantial concerns, and unveiling active species is crucial to rational design of bifunctional catalysts for ORR and OER. Herein, a hybrid of metal-rich nickel phosphides strongly coupled with heteroatom-doped carbon ( $\text{Ni}_x\text{P-NP-C}$ ) is constructed by a facile pyrolysis combined with in-situ phosphorization of MOFs. This unique hybrid exhibits superior electrocatalytic activity and stability toward ORR and OER demonstrated by delightful high  $E_{onset}$  and  $E_{1/2}$  up to 0.90 and 0.76 V, respectively, along with a long-term stability. The resulting zinc-air battery shows an impressively small charge-discharge voltage gap and delivers a high power density of  $266 \text{ mW cm}^{-2}$ . The high catalytic performance of  $\text{Ni}_x\text{P-NP-C}$  can be ascribed to synergistic effect of metal-rich  $\text{Ni}_2\text{P}$  actives and heteroatoms doped porous carbon. Consequently, hybrid of carbon and metal phosphides may provide a meaningful reference for developing high performance oxygen catalysts in metal-air battery.

## 1. Introduction

With the considerable environmental problems and increasing demands for energy, it is urgent to develop the eco-friendly and high-efficient energy devices or sources [1–3]. Among them, the rechargeable Zn-air battery featuring zero carbon emission and high energy density ( $1084 \text{ W h kg}^{-1}$ ) has been considered as a promising candidate for next-generation electronics [4–6]. The sluggish kinetics of the oxygen reduction reaction (ORR) and oxygen evolution reaction (OER) as core and essential processes to air electrode, are extremely depended on the high-efficient catalysts [7–12]. Up to now, the precious metal (Pt, Ir and Ru) based materials are still the most effective catalysts [13–15]. However, the high cost along with the unbalance catalytic activity for ORR and OER greatly hinders the wide application of rechargeable Zn-air battery [16,17]. In the past decades, abundant carbon based nonprecious metal catalysts have already been developed and explored as the most potential alternatives [18,19]. The hybrids of metal compounds (oxides, sulfides, nitrides, et al.) [20–29] and carbon have been aroused great attention as boosting bifunctional oxygen catalysts, due to

their distinct surface properties, tailored electronic structure and high conductivity. Apart from the above compounds, the metal phosphides with the similar electronic structure as platinum-group-metal have triggered substantial concerns in recent years [30–35].

It has been well-known that composition difference can lead to a great change of electronic structures, leading to the formation of metallic, semiconducting and/or insulating phases. Most of P-rich metal phosphides as intrinsic semiconductors or insulators are usually unstable due to their electrons concentrated around the P atoms, and thus are not ideal choice for the energy storage and conversion applications. By contrast, metal-rich metal phosphides (i.e.  $\text{MP}$ ,  $\text{M}_2\text{P}$  and  $\text{M}_3\text{P}$ ) exhibit good electronic conductivity, attributing to the metallic character [36–39]. Metal phosphides have shown great potential materials as OER catalysts, and Kupka and Budniok in 1989 firstly reported that metal phosphides exhibited good catalytic activity for OER [40]. Among metal phosphides, the stoichiometric compositions and crystal phases played an important role in the OER activity of nickel phosphide with higher activity than that of cobalt phosphide [38,41,42]. Combined with the results of experiment and theoretical calculation, a direct comparison of

\* Corresponding author at: State Key Laboratory for Modification of Chemical Fibers and Polymer Materials, College of Environmental Science and Engineering, Donghua University, 2999 Ren'min North Road, Shanghai 201620, China.

E-mail address: [qiaojl@dhu.edu.cn](mailto:qiaojl@dhu.edu.cn) (J. Qiao).

the metal phosphide by Markovican et al. further suggested that the catalytic activity following the order of Ni > Co > Fe > Mn [43,44]. It has been reported that the chemical process during OER process is complicated and the oxide/oxyhydroxide can be generated due to the irreversible surface oxidation [45]. However, there are few work of metal phosphides as bifunctional catalysts for OER and ORR. Meanwhile, it is still lack of fundamental understanding of the active site and catalytic mechanism. Designing the robust metal phosphides and unveiling the underlying mechanism during the catalytic process are crucial to develop high performance non-precious metal based bifunctional ORR/OER catalysts in metal-air battery.

Herein, focusing on the performance improvement and mechanism exploration of the metal phosphides as bifunctional catalysts for ORR and OER, hybrids of heteroatoms-doped carbon with metal-rich nickel phosphides ( $\text{Ni}_x\text{P-NP-C}$ ) are fabricated by a pyrolysis combined with in-situ phosphorization process of the  $\text{NiZn}$ -MOFs. The structure of  $\text{Ni}_x\text{P}$  nanoparticles and morphology of the hybrids is controllably tailored via regulating the pyrolysis process. The  $\text{Ni}_x\text{P-NP-C}$  catalyst exhibits good bifunctional catalytic activity for ORR and OER, outperforming that of commercial Pt/C. The home-made Zn-air battery with  $\text{Ni}_x\text{P-NP-C}$  as cathode catalyst delivers a high power density and a robust charge-discharge stability. The high catalytic performance of the  $\text{Ni}_x\text{P-NP-C}$  can be mainly ascribed to the synergistic effect of the metal-rich  $\text{Ni}_x\text{P}$  active sites and heteroatoms doped carbon matrix, and the good conductivity and porosity characteristics of the carbon matrix favorable for the electron and charge transfer during the ORR/OER processes. The hybrid of the carbon and metal phosphide may provide a meaningful reference for developing high performance non-precious metal based bifunctional oxygen catalysts in metal-air battery.

## 2. Experimental

### 2.1. Synthesis of $\text{Ni}_x\text{P-NP-C}$

Bimetal  $\text{NiZn}$ -MOFs were synthesized via the 2-Methylimidazole as ligands and Zn and Ni nitrates (molar ratio = 1:1) dissolved in deionized water under room temperature. The typical synthesis process of the bimetal MOFs has been detailed introduced in the previous reported work [46]. The above obtained  $\text{NiZn}$ -MOFs were put into the tube furnace and the phosphorous precursor of  $\text{Na}_2\text{HPO}_4$  was placed in front of the  $\text{NiZn}$ -MOFs. The pyrolysis included two steps. The first step of 300 °C for 2 h with a heating rate of 2 °C/min was aimed to decomposition  $\text{Na}_2\text{HPO}_4$  into  $\text{PH}_3$  to realize the phosphorization of  $\text{NiZn}$ -MOFs. Then, the second step under high temperatures for 2 h with a heating rate of 5 °C/min was used to obtain the carbonization of  $\text{NiZn}$ -MOFs and evaporation of Zn species. Finally, the hybrids of  $\text{Ni}_x\text{P}$  embedded into the N,P-doped porous carbon ( $\text{Ni}_x\text{P-NP-C}$ ) were obtained at the temperature of 800, 900 and 1000 °C during the second step, named  $\text{Ni}_x\text{P-NP-C800}$ ,  $\text{Ni}_x\text{P-NP-C900}$  and  $\text{Ni}_x\text{P-NP-C1000}$ , respectively.

### 2.2. Characterization

The morphology the obtained hybrids of  $\text{Ni}_x\text{P}$  embedded into the N,P-doped porous carbon based materials was determined via the Field Emission Transmission Electron Microscopy (FETEM, JEM-2100 F). The composition and corresponding element distribution of the materials were detected by the Energy Dispersive Spectroscopic (EDS). The microstructure and crystallization of the obtained powders were investigated via the X-Ray diffraction (XRD), and the Raman spectra was used to analysed the phase composition. The pore structural information of the materials, including the specific surface area and pore size distribution, was explored via the  $\text{N}_2$  sorption measurement (Micromeritics Tristar 3000) preformed at 77 K. The chemical and elemental composition of the obtained samples was systematically determined by the X-ray Photoelectron Spectroscopic (XPS, Thermo Fisher Scientific 250xi).

### 2.3. Electrochemical tests

The electrochemical properties of the obtained  $\text{Ni}_x\text{P-NP-C800}$ ,  $\text{Ni}_x\text{P-NP-C900}$  and  $\text{Ni}_x\text{P-NP-C1000}$  as bifunctional oxygen catalysts for oxygen reduction reaction (ORR) and oxygen evolution reaction (OER) were investigated via the standard three-electrode cell equipped on a CHI Electrochemical Station (760D). A mirror-smooth glassy carbon (GC) rotating ring disk electrode (RRDE, PINE, PA, USA) with a surface area of 0.2475  $\text{cm}^2$  was used as the substrate for the working electrode, along with a reference electrode of saturated calomel electrode (SCE). For the working electrode, the catalyst (2 mg) was dispersed into the mixture composed of isopropyl alcohol and 0.5 wt. % Nafion solution (400 and 100  $\mu\text{L}$ , respectively), and the uniform catalyst ink was obtained by ultrasonic for 40 min 12.4  $\mu\text{L}$  of ink was drop-casted onto the pre-cleaned GC surface with a 200  $\mu\text{g cm}^{-2}$  loading of the obtained catalysts, and then natural dried at room temperature. Prior to the electrochemical tests, the electrolyte medium was purged with high purity  $\text{N}_2$  or  $\text{O}_2$  for at least 30 min to guarantee all electrochemical tests to be performed in either  $\text{N}_2$ -saturated or  $\text{O}_2$ -saturated electrolytic environment. For better estimation of catalytic performance of the obtained catalysts, the commercial 20 % Pt/C (purchased from Johnson Matthey) and  $\text{IrO}_2$  were also chosen as bifunctional catalyst for ORR and OER. The stability of the catalysts was tested in the potential range from –0.5–0.2 V for 3000 cycles. And also, the durability was studied at constant current density of 20  $\text{mA cm}^{-2}$  for 12 h. All of the potentials during the electrochemical tests were converted into the reversible hydrogen electrode (RHE) by using the Eq. (1):

$$E(\text{RHE}) = E(\text{SCE}) + E^\theta(\text{SCE}) + 0.059pH \quad (1)$$

According to the disk current ( $I_d$ ) and ring current ( $I_r$ ) determined by the RRDE measurements, the  $\text{H}_2\text{O}_2$  yield ( $\text{H}_2\text{O}_2\ %$ ) and the corresponding electron transfer number ( $n$ ) can be calculated with the following equations of (2) and (3):

$$\text{H}_2\text{O}_2\% = 100 \times \frac{2I_r/N}{I_d + I_r/N} \quad (2)$$

$$n = \frac{4I_d}{I_d + I_r/N} \quad (3)$$

Where  $N = 0.37$  calibrated in 0.1 M KOH with a 10 mM  $\text{K}_3\text{Fe}(\text{CN})_6$  electrolyte, represents the current collection efficiency of the Pt ring.

The electrocatalytic properties of the obtained catalysts in the rechargeable Zn-air battery were investigated by a home-made electrochemical cell. The ink composed of the catalysts, isopropyl alcohol and 0.5 wt. % Nafion solution was prepared under the same dose and procedure mentioned above. The catalyst was sprayed onto the pre-treated carbon fiber paper (Toray TGP-H-090) as the air electrode with a loading of 1.0  $\text{mg cm}^{-2}$ . A polished Zn plate (99.99 %, 1.0 mm) was chosen as the anode paired with the air electrode in 6.0 M KOH electrolyte. The discharge polarization plots and power density were determined by a galvanodynamic method with the current density ranging from 0 to 1800  $\text{mA cm}^{-2}$  at room temperature. Electrochemical Impedance Spectroscopy (EIS) test was carried out with a standard three-electrode system equipped in a CHI760D workstation, and the AC voltage and amplitude were recorded at 1.1 V and 20 mV, respectively, with the frequency range from 100 kHz to 0.1 Hz. The discharge-charge cycling stability of the assembled rechargeable Zn-air battery was tested at the current density of the 2 and 5  $\text{mA cm}^{-2}$ , respectively.

## 3. Results and discussion

### 3.1. Synthesis and characterization of the $\text{Ni}_x\text{P-NP-C}$ hybrid

The hybrids of the  $\text{Ni}_x\text{P}$  nanoparticles embedded into the N,P-doped porous carbon ( $\text{Ni}_x\text{P-NP-C}$ ) is fabricated from MOFs precursors under

different pyrolysis temperature, as schematically illustrated in Fig. 1a. Briefly, the hexagonal NiZn-MOFs (Fig. S1), similar to other bimetal-MOFs given in our previous work [46], are first synthesized from the mixed solution of the metal salts and organic ligands under room temperature (step I). And then, three kinds of  $\text{Ni}_x\text{P-NP-C}$  hybrids can be obtained with NiZn-MOFs and  $\text{Na}_2\text{HPO}_4$  as precursors and phosphorous source, respectively, after second thermal treated at temperature from 800 to 1000 °C (step II, III and IV). Taking the advantages of the confinement and spatial isolation effects of bimetal MOFs, the metal based nanoparticles would be trapped and encapsulated growth in the cages of MOFs [47,48]. During the pyrolysis process, the  $\text{Ni}^{2+}$  gradually gathers to form Ni based nanoparticles anchored on the carbon matrix along with the thermal evaporation of the Zn species. The phosphide source placed before the NiZn-MOFs, is decomposed into  $\text{PH}_3$  species which then react with the NiZn-MOFs to promote the in-situ formation of  $\text{Ni}_x\text{P}$  nanoparticles and P doping into the carbon matrix. At the same time, the organic frameworks of the NiZn-MOFs are gradually carbonized, with an increase of the crystallization degree of Ni based phosphides. Meanwhile, the dual metal (Zn and Ni) sites can expand the adjacent distances between two Ni sites, allowing the formation of the small  $\text{Ni}_x\text{P}$  nanoparticles supported on porous carbon matrix.

The morphology of the obtained  $\text{Ni}_x\text{P-NP-C}$  hybrids is observed by TEM as shown in Figs. 1b-d. Under low temperature of 800 °C, it can be clearly seen that large particles are gathered together, which may be attributed to the Ni and unevaporated Zn based particles. With the temperature increased to 900 °C, the fabricated  $\text{Ni}_x\text{P-NP-C}$  hybrid demonstrated an ordered morphological characteristic featuring small nanoparticles uniformly dispersed on the carbon matrix. Whereas, with the thermal temperature continually increased to a higher temperature of 1000 °C, size of the particles increases rapidly, ascribing to the migration and aggregation of the Ni based nanoparticles under extremely high temperature. Based the analysis of the morphology characteristics, it can be concluded that  $\text{Ni}_x\text{P-NP-C}$  hybrids featuring uniformly dispersed small  $\text{Ni}_x\text{P}$  nanoparticles would be constructed under an optimized pyrolysis process.

The morphology of the  $\text{Ni}_x\text{P-NP-C900}$  is observed simultaneously by TEM under different resolutions, given in Figs. 2a-c, which further

confirms that the  $\text{Ni}_x\text{P}$  nanoparticles are uniformly dispersed in carbon matrix. From the HRTEM of  $\text{Ni}_x\text{P-NP-C900}$  hybrid in the inset of Fig. 2c, obvious lattice fringes can be observed with a spacing of 2.2 Å, assigned to the (111) plane of  $\text{Ni}_2\text{P}$  nanoparticles. Additionally, the carbon matrix demonstrates a porous feature, derived from the porous structure of the MOFs precursors. The element composition of the obtained  $\text{Ni}_x\text{P-NP-C900}$  hybrid is detected via the EDS as shown in Fig. S2. Strong signal of Ni and P can be remarkably observed, ascribing to the  $\text{Ni}_x\text{P}$  nanoparticles. Meanwhile, the element mappings in Fig. 2d and Fig. S3 confirm the uniform dispersion of Ni, P and N in the carbon matrix. More importantly, the dispersion of Ni and P illustrates a perfect overlap, further confirming the formation of  $\text{Ni}_x\text{P}$ .

The crystal structure of the as-synthesized hybrid is investigated by XRD. The pyrolysis temperature plays a great influence on the phase structure of the NiZn-MOFs derived metal phosphide nanoparticles. Fig. 2e shows the XRD patterns of the  $\text{Ni}_x\text{P-NP-C}$  hybrids treated at the temperature range from 800 to 1000 °C. For the  $\text{Ni}_x\text{P-NP-C800}$ , a series of the diffraction peaks can be detected at 14.4°, 20.9°, 26.3°, 28.0°, 29.7°, 31.1°, 34.8°, and so on, belonging to the (−111), (−112), (−312), (310), (022), (−313) and (400) crystalline phases of  $\text{Zn}_2(\text{PO}_3)_4$  (PDF: 21-1489), respectively. Besides, the above peaks may also be assigned to  $\text{Ni}(\text{PO}_3)_2$  (PDF: 28-0708). The existence of Zn based phosphates indicates that the uncompleted evaporation of the Zn species in the MOFs precursors, further explaining the formation of the large particles supported on the carbon matrix at low thermal temperature. By contrast, the hybrids fabricated at high temperature ( $\text{Ni}_x\text{P-NP-C900}$  and  $\text{Ni}_x\text{P-NP-C1000}$ ) demonstrate notably different diffraction peaks at 40.7°, 47.4°, 44.6°, 54.2°, 55.0° and 74.8°, which can be assigned to the planes of (111), (210), (201), (300), (211) and (400) for  $\text{Ni}_2\text{P}$  (PDF: 74-1385). The HRTEM image (inset image in Fig. 2c) exhibit lattice spacing of approximately 2.2 Å, which can be assigned to the (111) plane of  $\text{Ni}_2\text{P}$  nanoparticles. The elevated thermal temperature can promote the decomposition of  $\text{Zn}_2(\text{PO}_3)_4$  and evaporation of Zn, resulting in the generation of the  $\text{Ni}_2\text{P}$  nanoparticles embedded onto the porous carbon matrix. Notably, the strength of the diffraction peaks for the  $\text{Ni}_x\text{P-NP-C1000}$  is much higher than these of  $\text{Ni}_x\text{P-NP-C900}$ , attributing to the high temperature which can facilitate the grain growth of the  $\text{Ni}_2\text{P}$

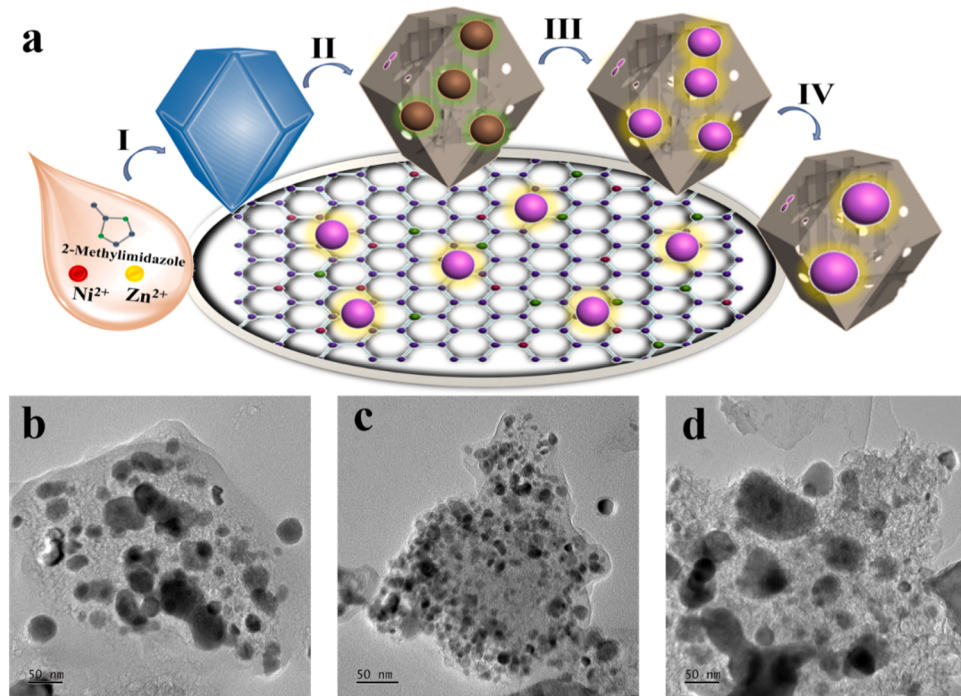


**Fig. 1.** Schematic illustration of the fabrication of the hybrids of  $\text{Ni}_x\text{P}$  embedded into the N,P-doped porous carbon (a). The TEM morphology of the hybrids synthesized under different pyrolysis temperature of 800, 900 and 1000 °C, respectively (b, c and d).

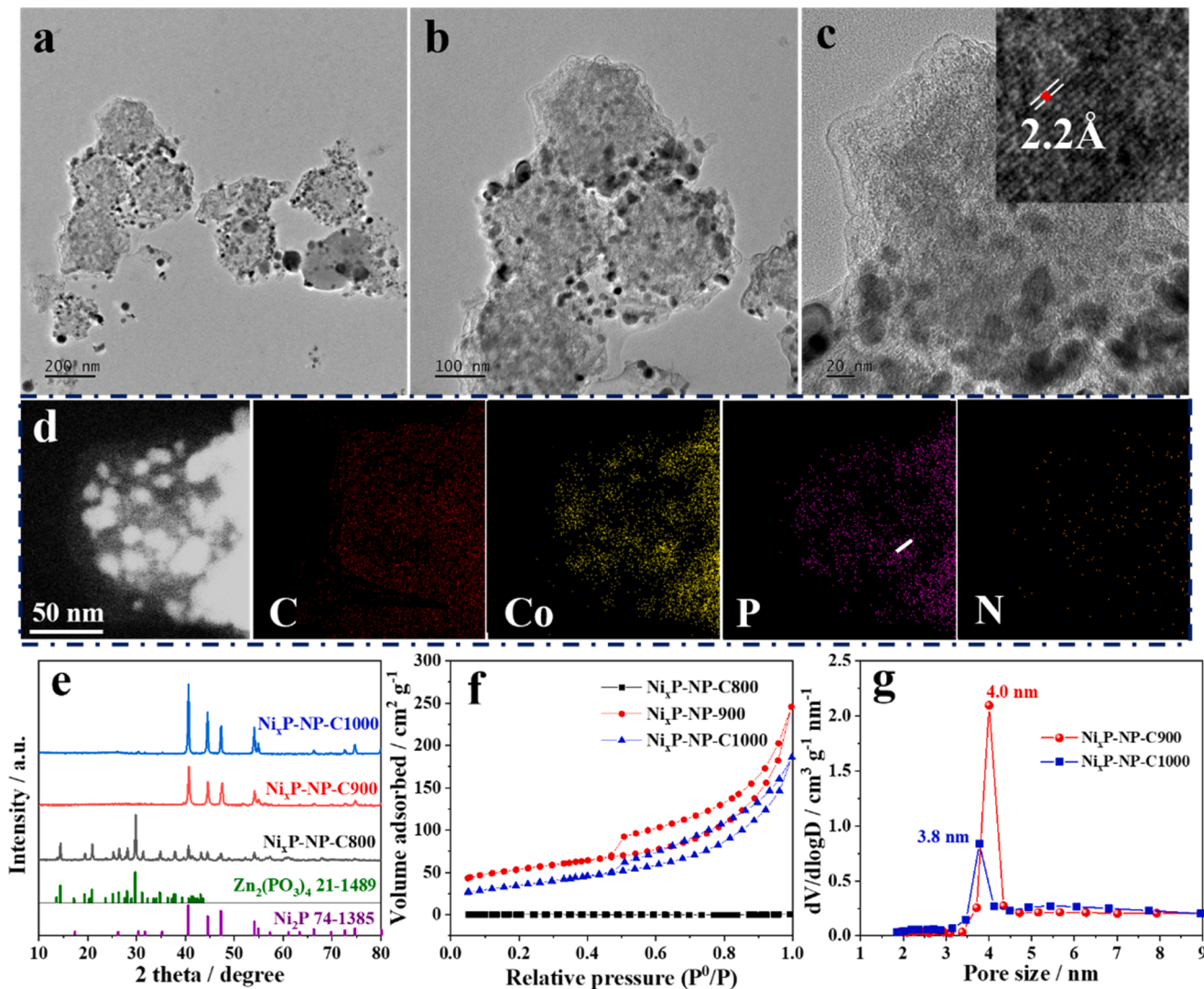


**Fig. 2.** The TEM morphology of the  $\text{Ni}_x\text{P-NP-C900}$  (a, b and c), The inset image in Fig. 2c is the HRTEM of the  $\text{Ni}_2\text{P}$ . (d) The element distribution of the  $\text{Ni}_x\text{P-NP-C900}$ , including C, Co, P and N. (e) XRD spectra of the  $\text{Ni}_x\text{P-NP-C800}$ ,  $\text{Ni}_x\text{P-NP-C900}$  and  $\text{Ni}_x\text{P-NP-C1000}$ . (f and g) The plots of surface area and pore size distribution of the hybrids.

nano-particles, consisting with the results of the morphology in Fig. 1c and d.

The pore structural parameters are characterized via the  $\text{N}_2$  adsorption-desorption measurements, and the BET surface area and pore size distribution of the hybrids are plotted in Fig. 2f and g. For  $\text{Ni}_x\text{P-NP-C900}$  and  $\text{Ni}_x\text{P-NP-C1000}$ , the isotherms can be identified as type-IV featuring distinct hysteresis loops, indicating the characteristics of mesoporous structure. The specific surface area and pore size of the  $\text{Ni}_x\text{P-NP-C900}$  are  $182.3 \text{ cm}^2 \text{ g}^{-1}$  and  $4.0 \text{ nm}$ , respectively, as listed in Table S1. Whereas, the specific surface area of  $\text{Ni}_x\text{P-NP-C1000}$  obviously decreases to  $126.2 \text{ cm}^2 \text{ g}^{-1}$ , attributing to the collapse of pore structure during the thermal treatment under a high temperature. It can draw a conclusion that the optimum thermal temperature is beneficial to the formation of the small  $\text{Ni}_2\text{P}$  nanoparticles embedded onto the mesoporous carbon matrix featuring high surface area, which may facilitate and enhance the electrocatalytic performance of the hybrids as bifunctional catalysts for oxygen reduction and oxygen evolution reactions.

To explore the effect of treatment temperature on the microstructure of the carbon based hybrids, the as-synthesized samples are determined by Raman spectroscopy. Typically, two main peaks at  $1350$  and  $1580 \text{ cm}^{-1}$  can be detected for all obtained hybrids, corresponding to disordered D and graphitic G bands, respectively, as shown in Fig. 3a.

The value of  $I_D/I_G$  as an important index to reflect the defect degree of carbon matrix, decreases from  $1.9$  for  $\text{Ni}_x\text{P-NP-C800}$  to  $1.3$  for  $\text{Ni}_x\text{P-NP-C1000}$ , indicating a decreased defect degree and an enhanced graphitic characteristic with the increase of thermal temperature. The high graphitic crystallinity of the carbon matrix can promote the conductivity of the hybrids, facilitating the electron transfer process and then endowing enhanced electrocatalytic activity. X-ray photoelectroscopic (XPS) is a reliable technique to analyze the element composition and understand the surface chemical features of the hybrids.  $\text{Ni}_x\text{P-NP-C900}$  is mainly composed of C, Ni, P, N and O, as shown in Fig. 3b.

In the high-resolution spectrum of C1s given in Fig. 3c, four main peaks can be fitted at the binding energy of  $283.7$ ,  $284.6$ ,  $285.8$  and  $288.6 \text{ eV}$ , assigning to C-C, C-N/C-O, C-N/C-P and C-OO, respectively. The appearance of the characteristic peaks of C-N and C-P demonstrates that the heteroatoms can be successfully doped into the carbon matrix during the pyrolysis process combined with in-situ phosphorization of the  $\text{NiZn}$ -MOFs. For the N1s in Fig. 3d, four typical bonding configurations can be obtained. Generally, the pyridinic-N and pyrrolic-N are doping N atoms bonded with two adjacent carbon atoms, at the bonding energy of  $401.7$  and  $400.4 \text{ eV}$ , respectively [49]. The peak at  $399.2 \text{ eV}$  is assigned to the graphitic-N species which substituted C atom in the

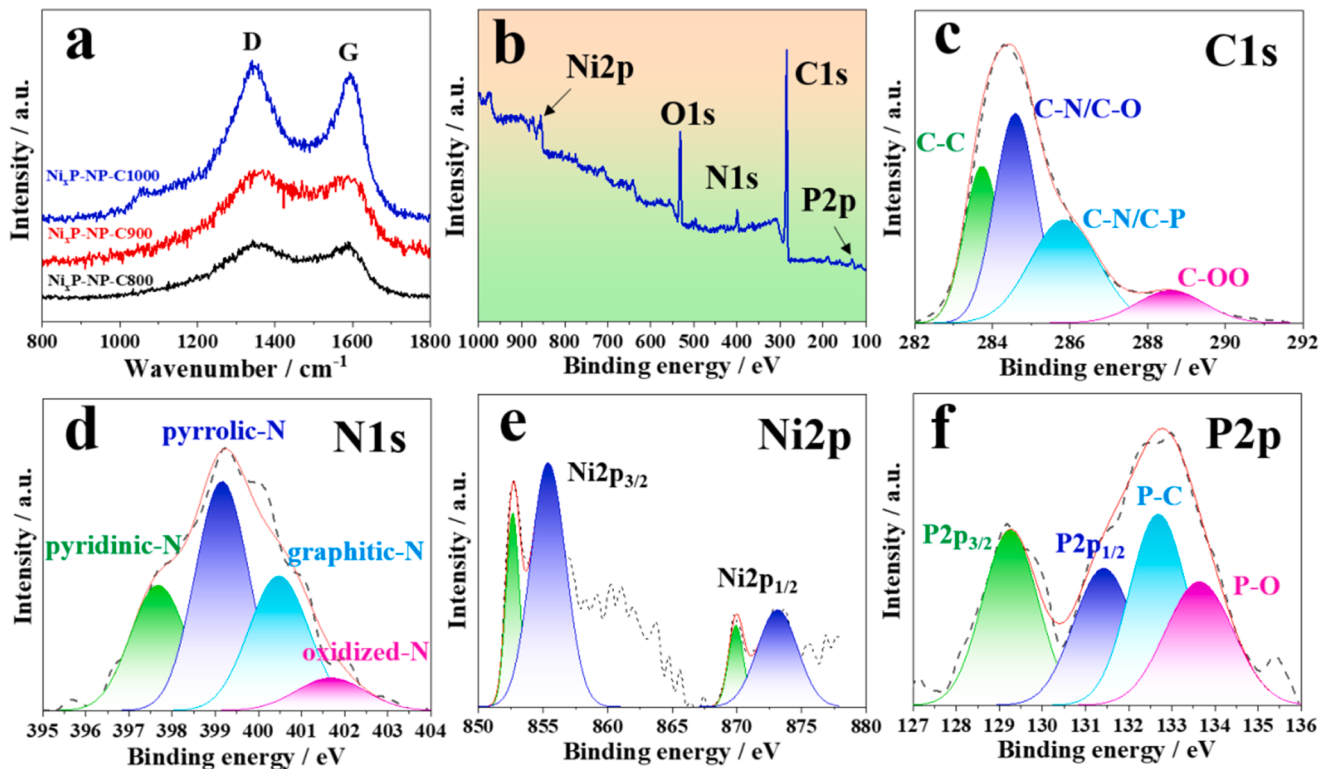


Fig. 3. (a) Raman spectra of the as-synthesized hybrids. (b) XPS spectra of  $\text{Ni}_x\text{P-NP-C900}$ . (c) C1s, (d) N1s, (e) Ni2p and (f) P2p of the  $\text{Ni}_x\text{P-NP-C900}$ .

hexagonal rings of the carbon matrix. Besides, the peak of oxidized-N species at 397.7 eV is resulted from the formation of nitrogen oxides during the exposure to the air. Additionally, it can be found that the pyridinic-N, pyrrolic-N and graphitic-N are the main species in the as-synthesized hybrid, which can endow a unique electrocatalytic

performance [50]. For the high-resolution of Ni2p spectrum in Fig. 3e, two dominating peaks at the binding energy of 852.6 and 870.1 eV are ascribed to the Ni-P species in  $\text{Ni}_2\text{P}$ , indicating the formation of the metal-rich Ni based phosphides. Besides, the peaks at 855.4 and 873.1 eV belong to the oxidized Ni arising from the surface oxidation of

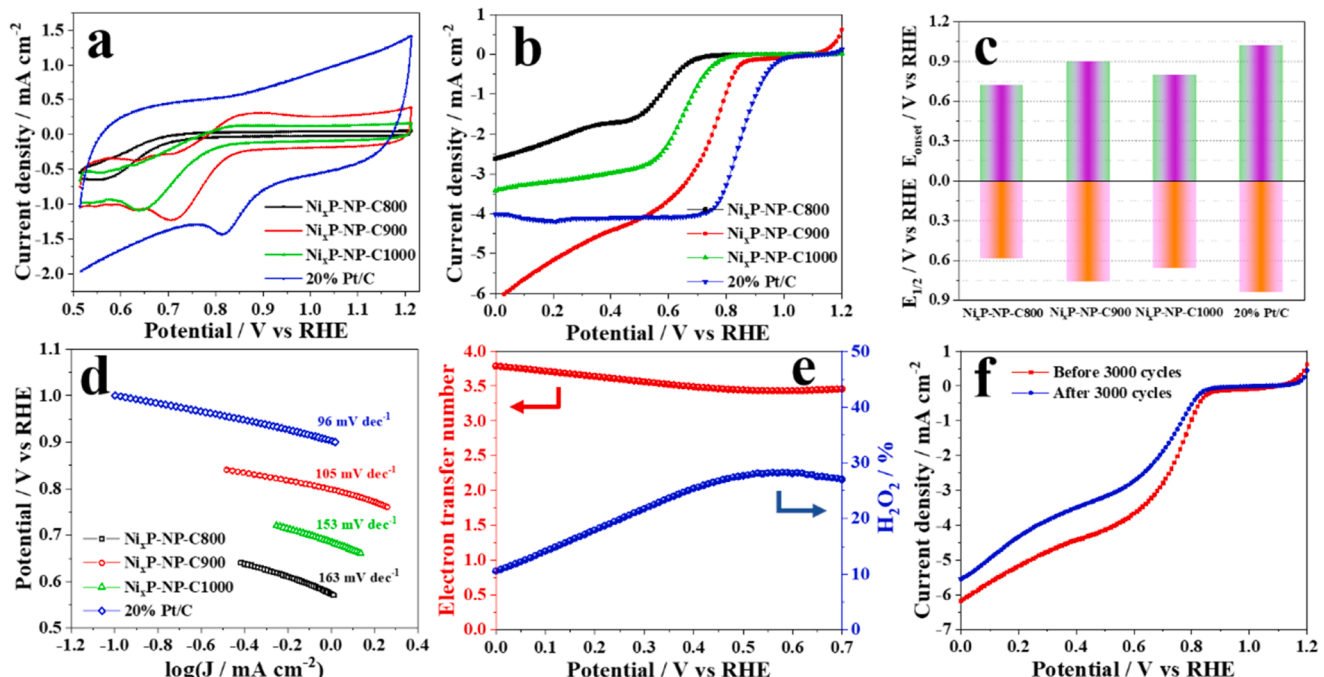


Fig. 4. (a) CV curves for ORR of the hybrids at  $\text{O}_2$ -saturated 0.1 M KOH at scanning rate of  $5 \text{ mV s}^{-1}$ , with a loading  $200 \text{ }\mu\text{g cm}^{-2}$ . (b) LSV curves for ORR at scanning rate of  $5 \text{ mV s}^{-1}$ , along with the rotation rate of 1600 rpm. (c) The bar graph of the onset potential and half-wave potential of the hybrids. (d) Tafel slope of the hybrids for ORR. (e) The electron transfer number ( $n$ ) and  $\text{H}_2\text{O}_2$  yield rate ( $\text{H}_2\text{O}_2 \%$ ) of  $\text{Ni}_x\text{P-NP-C900}$ . (f) The comparation of the LSV curves for ORR of  $\text{Ni}_x\text{P-NP-C900}$  before and after 3000 cycles.

$\text{Ni}_2\text{P}$  exposure in air. The P2p peaks given in Fig. 3f can be fitted into four peaks, and among them, the peaks at 129.2 and 131.4 eV can be ascribed to  $\text{P}2\text{p}_{1/2}$  and  $\text{P}2\text{p}_{3/2}$  of  $\text{Ni}_2\text{P}$ , respectively, which further confirms the formation of  $\text{Ni}_2\text{P}$  in the carbon matrix. Additionally, two other deconvoluted peaks at 132.7 and 133.6 eV can be assigned to P-C and P-O, respectively.

### 3.2. ORR performance of the $\text{Ni}_x\text{P-NP-C}$ electrocatalyst

To evaluate the bifunctional electrocatalytic performance of the as-synthesized hybrids for oxygen, the catalytic activity for oxygen reduction reaction (ORR) is firstly investigated in  $\text{O}_2$ -saturated 0.1 M KOH electrolytes. For the CV curves of  $\text{Ni}_x\text{P-NP-C800}$ , no obvious reduction peak can be seen in Fig. 4a, suggesting the low catalytic activity of the hybrid consisting of metal phosphates. Markedly, the strong reduction peaks can be clearly observed for  $\text{Ni}_x\text{P-NP-C900}$  and  $\text{Ni}_x\text{P-NP-C1000}$ , confirming the  $\text{Ni}_2\text{P}$  can be used as effectively active sites for ORR. It's worth noting that potential of the reduction peak for the  $\text{Ni}_x\text{P-NP-C900}$  is higher than that of the  $\text{Ni}_x\text{P-NP-C1000}$ , being closer to that the commercial 20 %Pt/C, confirming a higher catalytic activity of  $\text{Ni}_x\text{P-NP-C900}$  with uniform dispersed and exposure  $\text{Ni}_2\text{P}$  sites on the mesoporous carbon matrix. To further explore the catalytic performance of the hybrids, the linear sweep voltammograms (LSV) polarization curves are measured at a rotation rate of 1600 rpm and plotted in Fig. 4b. Typically,  $\text{Ni}_x\text{P-NP-C800}$  gives the lowest onset potential and half-wave potential, further confirming the poor catalytic activity for ORR. As expected, the hybrid of  $\text{Ni}_x\text{P-NP-C900}$  demonstrates high onset potential and half-wave potential up to 0.9 V and 0.76 V, respectively, much higher than these of the  $\text{Ni}_x\text{P-NP-C1000}$ , consisting with the results given in CV. The comprehensive comparison of the onset potential and half-wave potential of the hybrids and 20 %Pt/C is shown in Fig. 4c, from which it can be clearly seen that the  $\text{Ni}_x\text{P-NP-C900}$  exhibits a similar catalytic activity to 20 %Pt/C.

Tafel slope is an indicator of the reaction pathway and the rate-determining step during the ORR process [51]. The value of the Tafel

slope of the hybrids is calculated based on the LSV curves and plotted in Fig. 4d. Among the tested samples, the  $\text{Ni}_x\text{P-NP-C800}$  exhibits the highest Tafel slope ( $163 \text{ mV dec}^{-1}$ ), followed by  $\text{Ni}_x\text{P-NP-C1000}$  ( $153 \text{ mV dec}^{-1}$ ), suggesting that the slow ORR kinetics, which is consistent with the results of the CV and LSV. Notably, the Tafel slope of the  $\text{Ni}_x\text{P-NP-C900}$  is about  $105 \text{ mV dec}^{-1}$ , which is much more comparable to that of commercial 20 %Pt/C. The results indicate that  $\text{Ni}_x\text{P-NP-C900}$  displays a favorable ORR kinetics process among all the as-synthesized hybrids, further confirming the good electrocatalytic activity for ORR. The yield rate of  $\text{H}_2\text{O}_2$  ( $\text{H}_2\text{O}_2 \%$ ) and electron transfer number (n) of  $\text{Ni}_x\text{P-NP-C900}$  during the ORR process are calculated based the ring and disk current, as plotted in Fig. 4e. The average value of  $\text{H}_2\text{O}_2 \%$  and n in the voltage from 0 V to 0.7 V are about 20 % and 3.8, respectively, indicating that the ORR is controlled by a  $4\text{e}^-$  transfer process. To further explore the catalytic performance of  $\text{Ni}_x\text{P-NP-C900}$  for ORR, the long-term catalytic stability is investigated. From the LSV curves plotted in Fig. 4f, it can be found small difference of onset potential and half-wave potential between the catalyst for ORR before and after 3000 cycles, implying a slight degradation and good catalytic stability of  $\text{Ni}_x\text{P-NP-C900}$  for ORR.

### 3.3. OER performance of the $\text{Ni}_x\text{P-NP-C}$ electrocatalyst

As bifunctional catalysts for oxygen, the electrocatalytic performance of hybrids for oxygen evolution reaction (OER) is also investigated in the 0.1 M KOH electrolytes. According to the LSV curves for OER in Fig. 5a,  $\text{Ni}_x\text{P-NP-C800}$  exhibits the worst catalytic activity for OER, suggesting the hybrid obtained at low temperature of 800 °C is a poor bifunctional catalyst for ORR and OER. Delightfully,  $\text{Ni}_x\text{P-NP-C900}$  presents the best catalytic performance among all the as-synthesized hybrid, outstanding that of the commercial 20 %Pt/C. The potential at the current density of  $10 \text{ mA cm}^{-2}$  is a significant parameter to reflect the catalytic activity of the catalyst. The hybrid of  $\text{Ni}_x\text{P-NP-C900}$  and  $\text{Ni}_x\text{P-NP-C1000}$ , consisting of  $\text{Ni}_2\text{P}$  embedded onto N,P co-doped porous carbon matrix, can be used as effective catalysts to boost the OER

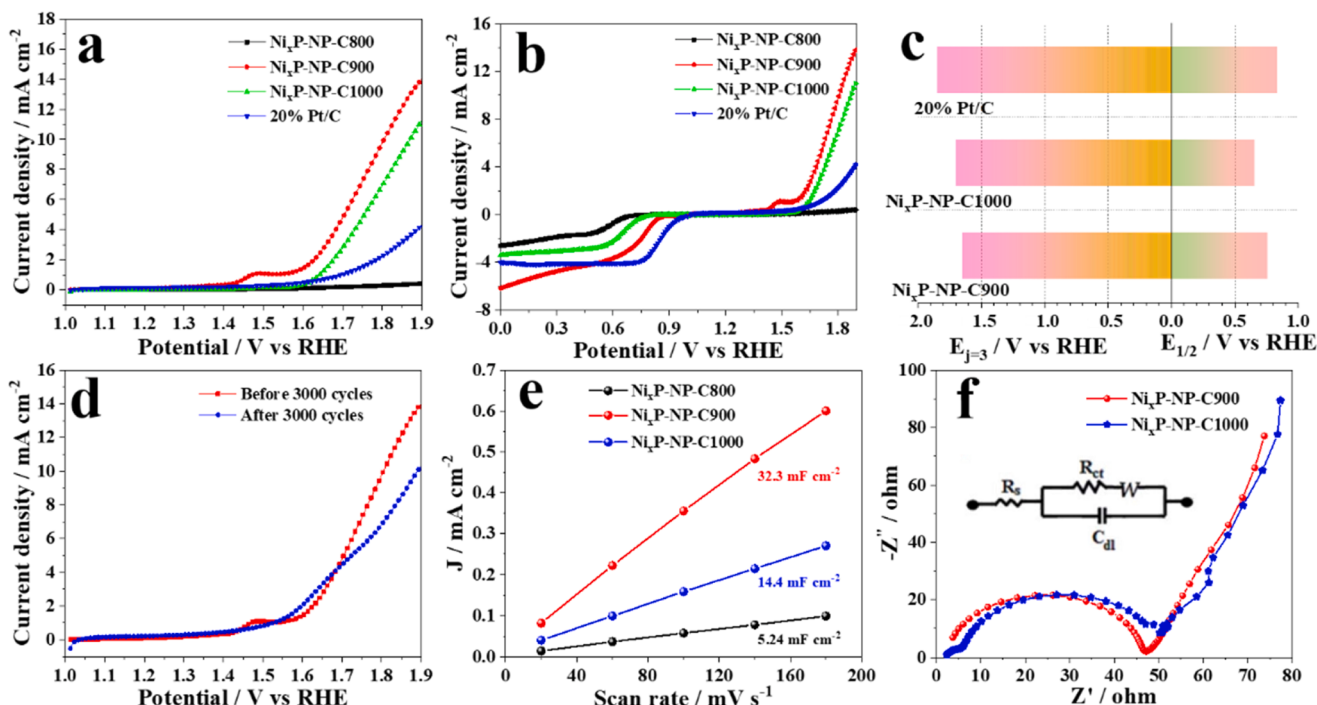


Fig. 5. (a) LSV curves for OER in  $\text{O}_2$ -saturated 0.1 M KOH at scanning rate of  $5 \text{ mV s}^{-1}$  and 1600 rpm, respectively. (b) Overall LSV curves of the hybrids  $\text{O}_2$ -saturated 0.1 M KOH. (c) The potential gap between the potential for OER at current density of  $3 \text{ mA cm}^{-2}$  and half-wave potential for ORR. (d) The comparison of the LSV curves for OER of  $\text{Ni}_x\text{P-NP-C900}$  before and after 3000 cycles. (e) The linear fitting plots of scan rates with capacitive current densities for the hybrids. (f) The Nyquist plots of  $\text{Ni}_x\text{P-NP-C900}$  and  $\text{Ni}_x\text{P-NP-C1000}$ . The inset shows the equivalent circuit diagram.

process. Whereas,  $\text{Ni}_x\text{P-NP-C900}$  can promote the OER at a much more negative potential, further illustrating a higher catalytic activity of  $\text{Ni}_x\text{P-NP-C900}$ . The potential gap ( $\Delta E$ ) between OER and ORR can be regarded as a unique descriptor to assess the overall catalytic activity of the bifunctional catalyst for ORR and OER. As shown in Fig. 5b,  $\text{Ni}_x\text{P-NP-C900}$  displays the best bifunctional catalytic activity among all the prepared hybrids, outperforming these of the commercial 20 % Pt/C and  $\text{IrO}_2$  (Fig. S5) catalysts. The value of  $\Delta E$  is plotted in Fig. 5c, and from which it can be clearly seen that  $\text{Ni}_x\text{P-NP-C900}$  demonstrates the smallest  $\Delta E$ , confirming the best bifunctional catalytic activity.

Similarly, Tafel slope of the hybrids for OER is calculated to evaluate the catalytic kinetics, as shown in Fig. S5. As expected,  $\text{Ni}_x\text{P-NP-C900}$  demonstrates the lowest Tafel slope, confirming that it can facilitate the OER process. Meanwhile, the results of the long-term catalytic stability after 3000 cycles (Fig. 5d), shows a negligible difference at the current density of  $10 \text{ mA cm}^{-2}$ , indicating an ignored degradation of  $\text{Ni}_x\text{P-NP-C900}$  during the OER process. Moreover, the catalytic performance of  $\text{Ni}_x\text{P-NP-C900}$  for ORR and OER after testing under constant current density of  $20 \text{ mA cm}^{-2}$  for 12 h have been done and overall LSV curves have been given in Fig. S6. From the compared curves, the catalytic activity of the hybrid decreases in different degrees for ORR and OER, attributing to the structural damage during the long-term catalytic process under a high current density. Furthermore, the electrochemical double layer capacitance ( $C_{dl}$ ) is generally proportional to the electrochemical active surface area (ECSA) [52,53], which can be used as the reference to investigate the catalytic activity of the catalyst. According to the CV curves scanning at different scanning rate range from 20 to  $180 \text{ mV s}^{-1}$  (Fig. S7),  $C_{dl}$  is calculated and plotted in Fig. 5e. Among all the as-synthesized hybrids,  $\text{Ni}_x\text{P-NP-C800}$  presents the smallest  $C_{dl}$ , indicating the minimal active surface area and further explaining the worst bifunctional catalytic activity. Notably, the  $C_{dl}$  of  $\text{Ni}_x\text{P-NP-C900}$  is two-fold of that the  $\text{Ni}_x\text{P-NP-C1000}$ , indicating a higher electrochemical active surface area. The electrochemical impedance spectroscopy (EIS) is detected to further verify the charge transport capability of the  $\text{Ni}_2\text{P}$

nanoparticles embedded on the carbon matrix, and the Nyquist plots are plotted in Fig. 5f. Compared with  $\text{Ni}_x\text{P-NP-C1000}$  ( $55 \Omega$ ), the hybrid of  $\text{Ni}_x\text{P-NP-C900}$  ( $46 \Omega$ ) demonstrate a much smaller charge transfer resistance ( $R_{ct}$ ), indicating a faster catalytic kinetics of  $\text{Ni}_x\text{P-NP-C900}$ . The plentiful active surface area can provide much more active sites for the electrocatalytic process, confirming the best bifunctional catalytic performance of  $\text{Ni}_x\text{P-NP-C900}$  for ORR and OER.

### 3.4. Application of $\text{Ni}_x\text{P-NP-C}$ as bifunctional cathode electrocatalyst for rechargeable Zn-air battery

A home-made rechargeable Zn-air battery equipped with polished Zn plates and carbon paper as anode and cathode, respectively, is used to evaluate the bifunctional electrocatalytic activity for ORR and OER, shown in Fig. 6a. The as-synthesized hybrid is sprayed onto carbon paper with a loading of  $1 \text{ mg cm}^{-2}$ . The polarization curves and power density of  $\text{Ni}_x\text{P-NP-C900}$  as cathode catalyst is plotted in Fig. 6b, and from which, it can be seen that the maximum power density of the battery is high up to  $266 \text{ mW cm}^{-2}$ , outperforming most reported metal phosphides based catalysts as listed in Table S2. Meanwhile, three light-emitting diodes (LED) can be lightened by three Zn-air batteries connected in series (Fig. 6c), implying the promising application of the obtained metal phosphides hybrid ( $\text{Ni}_x\text{P-NP-C900}$ ) in Zn-air battery. The long-term charge-discharge stability of the battery is determined via a LAND system, and the test results at the current density of 2 and  $5 \text{ mA cm}^{-2}$  are plotted in Fig. 6d. Impressively, the battery displays a small charge-discharge voltage gap of about  $50 \text{ mV}$  at  $5 \text{ mA cm}^{-2}$ . After 30 h, there is a negligible change of the discharge and charge voltage, indicating a robust stability of the hybrid as cathode catalyst in the battery. Additionally, the typical galvanostatic discharge curves at the current density of 10 and  $20 \text{ mA cm}^{-2}$  demonstrate that the batteries can be discharged for at least 70 and 45 h, respectively (Fig. 6e).

Combined with the structural analysis and the results of electrochemical experiments, the possible catalytic mechanism (Fig. 6f) of the

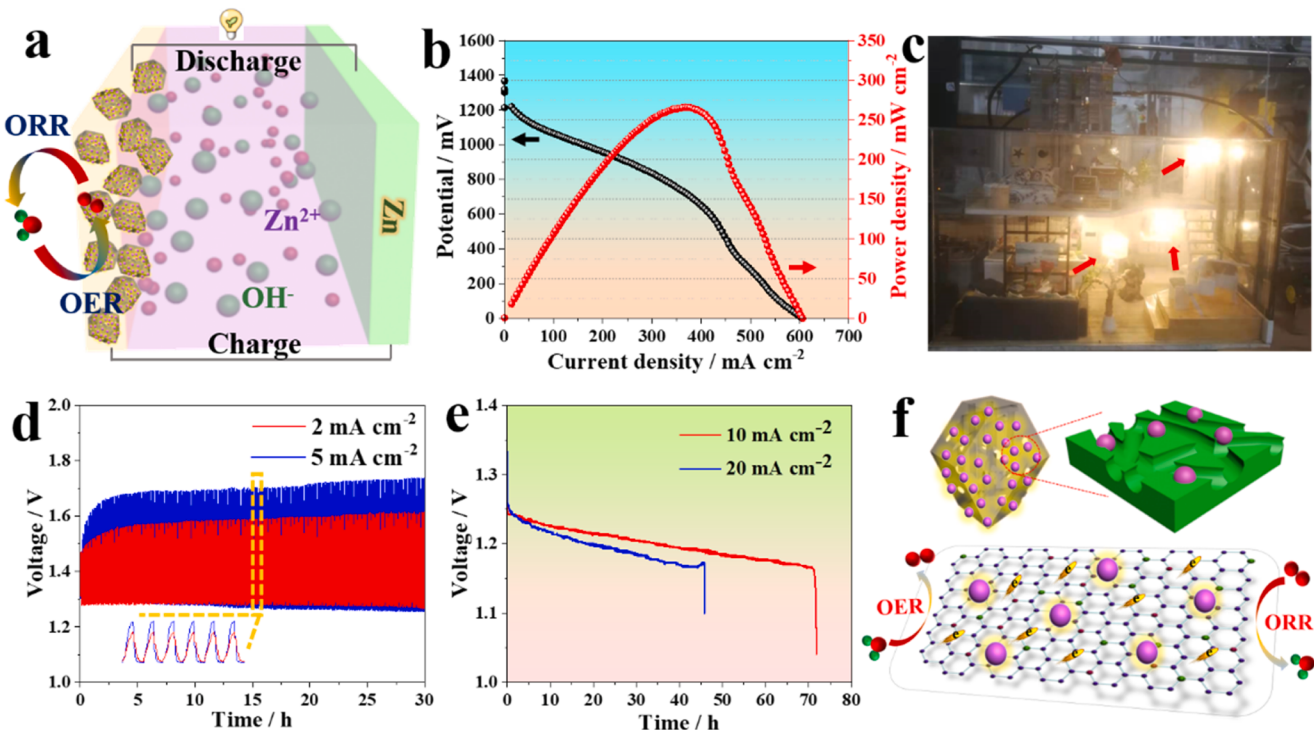


Fig. 6. (a) Home-made rechargeable Zn-air battery. (b) The polarization curves and power density of  $\text{Ni}_x\text{P-NP-C900}$  as cathode catalyst in Zn-air battery. (c) Photograph of LEDs powered by three  $\text{Ni}_x\text{P-NP-C900}$  based Zn-air battery in series. (d) The discharge-charge stability of the  $\text{Ni}_x\text{P-NP-C900}$  at the current density of 2 and  $5 \text{ mA cm}^{-2}$ . (e) The galvanostatic discharge curves at the current density of 10 and  $20 \text{ mA cm}^{-2}$ . (f) The bifunctional catalytic mechanism of the  $\text{Ni}_x\text{P-NP-C900}$  for ORR and OER.

as-synthesized hybrids as bifunctional catalysts for ORR and OER can be concluded as follows: 1) Metal-rich  $\text{Ni}_2\text{P}$  nanoparticles as the active sites to enhance the bifunctional catalytic activity for ORR and OER. More importantly, the uniformly dispersed small  $\text{Ni}_2\text{P}$  nanoparticles is extremely important to make full use of the active sites. 2) Co-doping of the heteroatoms (N and P) into the carbon skeleton introduce number of structural defect and change the electronic structure of the carbon matrix [54–57], resulting in the enrichment of the active sites and enhancement of the catalytic activity. 3) The high surface area and plentiful channel structure of the mesoporous carbon matrix can promote the migration of the intermediates during the catalytic process. Additionally, good conductivity of the carbon matrix is beneficial for the transfer of the electron, and then further accelerates the electrocatalytic reaction. In general, the synergistic effect of the above factors, that are enriched active sites ( $\text{Ni}_2\text{P}$  and defected carbon) and skeleton structural characteristics of high surface area and good conductivity, acts as the most important role to boost the bifunctional catalytic active for ORR and OER.

To further reveal the stability and in-depth understand the catalytic mechanism of the hybrid during catalytic process, the morphology, composition and microstructure of the  $\text{Ni}_x\text{P-NP-C900}$  hybrid after electrocatalytic tests are demonstrated in Fig. S8. From the TEM morphology of the hybrid as shown in Fig. S8a, no obvious change for the morphology can be observed, compared to the initial morphology in Figs. 1c and 2a. Meanwhile, the peaks in the XRD pattern of  $\text{Ni}_x\text{P-NP-C900}$  given in Fig. S8b, are mainly assigned to  $\text{Ni}_2\text{P}$  (PDF: 74–1385), indicating a negligible structural change of  $\text{Ni}_2\text{P}$  nanoparticles in  $\text{Ni}_x\text{P-NP-C900}$ . Thus, the durability of the  $\text{Ni}_x\text{P-NP-C900}$  hybrid as bifunctional oxygen catalyst in Zn-air battery can be ascribed to the good structural stability of the metal-rich  $\text{Ni}_2\text{P}$  active sites and maintenance of the pore framework of the porous carbon matrix after electrochemical tests.

#### 4. Conclusion

In summary, hybrids of heteroatoms-doped carbon with metal-rich nickel phosphides ( $\text{Ni}_x\text{P-NP-C}$ ) are fabricated by a pyrolysis combined with in-situ phosphorization process of the  $\text{NiZn}$ -MOFs. The structure of  $\text{Ni}_x\text{P}$  nanoparticles and morphology of the hybrids are controllably tailored via regulating the pyrolysis process. The  $\text{Ni}_x\text{P-NP-C}$  catalyst exhibits good catalytic activity for ORR with high  $E_{onset}$  and  $E_{1/2}$  up to 0.90 and 0.76 V (vs RHE), respectively, along with a long-term catalytic stability. Excitingly, the metal-rich  $\text{Ni}_x\text{P-NP-C}$  demonstrates a much lower potential for OER at the current density of  $10 \text{ mA cm}^{-2}$ , outperforming these of other two hybrids and even commercial Pt/C. The home-made Zn-air battery with  $\text{Ni}_x\text{P-NP-C}$  as cathode catalyst delivers a high power density of  $266 \text{ mW cm}^{-2}$ , as well as a robust charge-discharge stability. The high catalytic performance of the  $\text{Ni}_x\text{P-NP-C}$  can be mainly ascribed to the synergistic effect of the metal-rich  $\text{Ni}_2\text{P}$  actives and heteroatoms doped carbon matrix, and the good conductivity and porosity characteristics favorable for the electron and charge transfer during the ORR/OER processes.

#### CRediT authorship contribution statement

**Yongxia Wang:** Writing – original draft, Investigation, Methodology, Formal analysis. **Jiaxi Liu:** Investigation, Writing – review & editing. **Tuo Lu:** Methodology, Investigation, Data curation. **Rui He:** Methodology, Investigation. **Nengneng Xu:** Conceptualization, Project administration. **Jinli Qiao:** Supervision, Project administration, Writing – review & editing, Funding acquisition.

#### Declaration of Competing Interest

The authors declare that they have no known competing financial interests or personal relationships that could have appeared to influence

the work reported in this paper.

#### Data availability

No data was used for the research described in the article.

#### Acknowledgement

This work is financially supported by the “Scientific and Technical Innovation Action Plan” Hong Kong, Macao and Taiwan Science &Technology Cooperation Project of Shanghai Science and Technology Committee (19160760600) and National Natural Science Foundation of China (21972017).

#### Appendix A. Supporting information

Supplementary data associated with this article can be found in the online version at doi:10.1016/j.apcatb.2022.122041.

#### References

- [1] M. Wu, E. Zhang, Q. Guo, Y. Wang, J. Qiao, K. Li, P. Pei, N/S-Me (Fe, Co, Ni) doped hierarchical porous carbons for fuel cell oxygen reduction reaction with high catalytic activity and long-term stability, *Appl. Energy* 175 (2016) 468–478, <https://doi.org/10.1016/j.apenergy.2016.03.065>.
- [2] J. Ren, Y. Huang, H. Zhu, B. Zhang, H. Zhu, S. Shen, G. Tan, F. Wu, H. He, S. Lan, X. Xia, Q. Liu, Recent progress on MOF-derived carbon materials for energy storage, *Carbon Energy* 2 (2020) 176, <https://doi.org/10.1002/cey2.44>.
- [3] X. Feng, M. Ouyang, X. Liu, L. Lu, Y. Xia, X. He, Thermal runaway mechanism of lithium ion battery for electric vehicles: a review, *Energy Stor. Mater.* 10 (2018) 246–267, <https://doi.org/10.1016/j.ensm.2017.05.013>.
- [4] Y. Li, M. Gong, Y. Liang, J. Feng, J.E. Kim, H. Wang, G. Hong, B. Zhang, H. Dai, Advanced zinc-air batteries based on high-performance hybrid electrocatalysts, *Nat. Commun.* 4 (2013) 1805, <https://doi.org/10.1038/ncomms2812>.
- [5] M. Wu, G. Zhang, M. Wu, J. Prakash, S. Sun, Rational design of multifunctional air electrodes for rechargeable Zn-Air batteries: recent progress and future perspectives, *Energy Stor. Mater.* 21 (2019) 253–286, <https://doi.org/10.1016/j.ensm.2019.05.018>.
- [6] G.J. Liang, C.Y. Zhi, A reversible Zn-metal battery, *Nat. Nanotechnol.* 16 (2021) 854–855, <https://doi.org/10.1038/s41565-021-00908-1>.
- [7] Q. Tang, L. Wang, M. Wu, N. Xu, L. Jiang, J. Qiao, Achieving high-powered Zn/air fuel cell through N and S co-doped hierarchically porous carbons with tunable active-sites as oxygen electrocatalysts, *J. Power Sources* 365 (2017) 348–353, <https://doi.org/10.1016/j.jpowsour.2017.08.102>.
- [8] Q. Lu, X. Zou, K. Liao, R. Ran, W. Zhou, M. Ni, Z. Shao, Direct growth of ordered N-doped carbon nanotube arrays on carbon fiber cloth as free-standing and binder-free air electrode for flexible quasi-solid-state rechargeable Zn-Air batteries, *Carbon Energy* 2 (2020) 461–471, <https://doi.org/10.1002/cey2.50>.
- [9] H.G. Li, J. Wang, R.J. Qi, Y.F. Hu, J. Zhang, H.B. Zhao, J.J. Zhang, Y.F. Zhao, Enhanced Fe 3d delocalization and moderate spin polarization in Fesingle bondNi atomic pairs for bifunctional ORR and OER electrocatalysis, *Appl. Catal. B Environ.* 285 (2021), 119778, <https://doi.org/10.1016/j.apcatb.2020.119778>.
- [10] C.C. Weng, J.T. Ren, H.Y. Wang, X.W. Lv, Y.J. Song, Y.S. Wang, L. Chen, W. W. Tian, Z.Y. Yuan, Triple-phase oxygen electrocatalysis of hollow spherical structures for rechargeable Zn-Air batteries, *Appl. Catal. B Environ.* 307 (2022), 121190, <https://doi.org/10.1016/j.apcatb.2022.121190>.
- [11] K. Song, Y. Feng, X. Zhou, T. Qin, X. Zou, Y. Qi, Z. Chen, J. Rao, Z. Wang, N. Yue, X. Ge, W. Zhang, W. Zheng, Exploiting the trade-offs of electron transfer in MOF-derived single Zn/Co atomic couples for performance-enhanced zinc-air battery, *Appl. Catal. B: Environ.* 316 (2022), 121591, <https://doi.org/10.1016/j.apcatb.2022.121591>.
- [12] C.-X. Zhao, J.-N. Liu, J. Wang, C. Wang, X. Guo, X.-Y. Li, X. Chen, L. Song, B.-Q. Li, Q. Zhang, A clicking confinement strategy to fabricate transition metal single-atom sites for bifunctional oxygen electrocatalysis, *Sci. Adv.* 8 (2022) 5091, <https://doi.org/10.1126/sciadv.abn5091>.
- [13] N. Alonso-Vante, Y. Feng, H. Yang, Novel non-precious metal electrocatalysts for oxygen electrode reactions, *Catalysts* 9 (2019) 731, <https://doi.org/10.3390/cata9090731>.
- [14] W.H. Lee, Y.J. Ko, J.H. Kim, C.H. Choi, K.H. Chae, H. Kim, Y.J. Hwang, B.K. Min, P. Strasser, H.S. Oh, High crystallinity design of Ir-based catalysts drives catalytic reversibility for water electrolysis and fuel cells, *Nat. Commun.* 12 (2021) 4271, <https://doi.org/10.1038/s41467-021-24578-8>.
- [15] J.J. Zhao, C.H. Fu, K. Ye, Z. Liang, F.L. Jiang, S.Y. Shen, X.R. Zhao, L. Ma, Z. Shadique, X.M. Wang, J.L. Zhang, K. Jiang, Manipulating the oxygen reduction reaction pathway on Pt-coordinated motifs, *Nat. Commun.* 13 (2022) 685, <https://doi.org/10.1038/s41467-022-28346-0>.
- [16] M. Wu, G. Zhang, M. Wu, J. Prakash, S. Sun, Rational design of multifunctional air electrodes for rechargeable Zn-Air batteries: recent progress and future perspectives, *Energy Stor. Mater.* 21 (2019) 253–286, <https://doi.org/10.1016/j.ensm.2019.05.018>.

[17] Y.G. Zhang, Y.P. Deng, J.Y. Wang, Y. Jiang, G.L. Cui, L.L. Shui, A.P. Yu, Xin Wang, Z.W. Chen, Recent progress on flexible Zn-air batteries, *Energy Stor. Mater.* 35 (2021) 538–549, <https://doi.org/10.1016/j.ensm.2020.09.008>.

[18] Y. Feng, K. Song, W. Zhang, X. Zhou, S.J. Yoo, J.-G. Kim, S. Qiao, Y. Qi, X. Zou, Z. Chen, T. Qin, N. Yue, Z. Wang, D. Li, W. Zheng, Efficient ORR catalysts for zinc-air battery: biomass-derived ultra-stable Co nanoparticles wrapped with graphitic layers via optimizing electron transfer, *J. Energy Chem.* 70 (2022) 211–218, <https://doi.org/10.1016/j.jpcatb.2022.121591>.

[19] V. Jose, J.M.V. Nsanzimana, H. Hu, J. Choi, X. Wang, J.-M. Lee, Highly efficient oxygen reduction reaction activity of N-doped carbon–cobalt boride heterointerfaces, *Adv. Energy Mater.* 11 (2021) 2100157.

[20] J. Chen, C. Fan, X. Hu, C. Wang, Z. Huang, G. Fu, J.-M. Lee, Y. Tang, Hierarchically porous Co/CoxMy (M = P, N) as an efficient Mott–Schottky electrocatalyst for oxygen evolution in rechargeable Zn–air batteries, *Small* 15 (2019) 1901518, <https://doi.org/10.1002/smll.201901518>.

[21] H. Li, S. Kelly, D. Guevarra, Z.B. Wang, Y. Wang, J.A. Haber, M. Anand, G.T.K. Gunasooriya, C.S. Abraham, S. Vijay, J.M. Gregoire, J.K. Nørskov, Analysis of the limitations in the oxygen reduction activity of transition metal oxide surfaces, *Nat. Catal.* 4 (2021) 463–468, <https://doi.org/10.1038/s41929-021-00618-w>.

[22] G. Fu, X. Yan, Y. Chen, L. Xu, D. Sun, J.-M. Lee, Y. Tang, Boosting bifunctional oxygen electrocatalysis with 3D graphene aerogel-supported Ni/MnO particles, *Adv. Mater.* 30 (2018) 1704609, <https://doi.org/10.1002/adma.201704609>.

[23] X. Hu, Y. Chen, M. Zhang, G. Fu, D. Sun, J.-M. Lee, Y. Tang, Alveolate porous carbon aerogels supported Co9S8 derived from a novel hybrid hydrogel for bifunctional oxygen electrocatalysis, *Carbon* 144 (2019) 557–566, <https://doi.org/10.1016/j.carbon.2018.12.099>.

[24] Y.H. Tian, L. Xu, M. Li, D. Yuan, X.H. Liu, J.C. Qian, Y.H. Dou, J.X. Qiu, S.Q. Zhang, Interface engineering of CoS/CoO@N-doped graphene nanocomposite for high-performance rechargeable Zn–air batteries, *Nano-Micro Lett.* 13 (2021) 3, <https://doi.org/10.1007/s40820-020-00526-x>.

[25] P. Prabhu, V. Jose, J.-M. Lee, Design strategies for development of TMD-based heterostructures in electrochemical energy systems, *Matter* 2 (2020) 526–553, <https://doi.org/10.1016/j.matt.2020.01.001>.

[26] Z. Jin, P. Li, D. Xiao, Metallic Co<sub>2</sub>P ultrathin nanowires distinguished from CoP as robust electrocatalysts for overall water-splitting, *Green. Chem.* 18 (2016) 1459–1464, <https://doi.org/10.1039/c5gc02462e>.

[27] M.J. Wu, G.X. Zhang, J.L. Qiao, N. Chen, W.F. Chen, S.H. Sun, Ultra-long life rechargeable zinc-air battery based on high-performance trimetallic nitride and NCNT hybrid bifunctional electrocatalysts, *Nano Energy* 61 (2019) 86–95, <https://doi.org/10.1016/j.nanoen.2019.04.031>.

[28] H. Wang, J. Li, K. Li, Y. Lin, J. Chen, L. Gao, V. Nicolosi, X. Xiao, J.-M. Lee, Transition metal nitrides for electrochemical energy applications, *Chem. Soc. Rev.* 50 (2021) 1354–1390, <https://doi.org/10.1039/D0CS00415D>.

[29] W. Liu, E. Hu, H. Jiang, Y. Xiang, Z. Weng, M. Li, Q. Fan, X. Yu, E.I. Altman, H. Wang, A highly active and stable hydrogen evolution catalyst based on pyrite-structured cobalt phosphosulfide, *Nat. Commun.* 7 (2016) 10771, <https://doi.org/10.1038/ncomms10771>.

[30] L. Feng, H. Vrubel, M. Bensimon, X. Hu, Easily-prepared dinickel phosphide (Ni<sub>2</sub>P) nanoparticles as an efficient and robust electrocatalyst for hydrogen evolution, *Phys. Chem. Chem. Phys.* 16 (2014) 5917–5921, <https://doi.org/10.1039/c4cp00482e>.

[31] Y.-H. Chung, K. Gupta, J.-H. Jang, H.S. Park, I. Jang, J.H. Jang, Y.-K. Lee, S.-C. Lee, S.J. Yoo, Rationalization of electrocatalysis of nickel phosphide nanowires for efficient hydrogen production, *Nano Energy* 26 (2016) 496–503, <https://doi.org/10.1016/j.nanoen.2016.06.002>.

[32] Y. Yu, J. Ma, C. Chen, Y. Fu, Y. Wang, K. Li, Y. Liao, L. Zheng, X. Zuo, General method for synthesis transition-metal phosphide/nitrogen and phosphide doped carbon materials with yolk-shell structure for oxygen reduction reaction, *ChemCatChem* 11 (2019) 1722–1731, <https://doi.org/10.1002/cctc.201801935>.

[33] S. Singh, D.C. Nguyen, N. HoonKim\*, J.H. Lee, Interface engineering induced electrocatalytic behavior in core-shelled CNTs@NiP2/NbP heterostructure for highly efficient overall water splitting, *Chem. Eng. J.* 442 (2022), 136120, <https://doi.org/10.1016/j.cej.2022.136120>.

[34] Y.F. Liu, B. Wang, Y.J. Lu, Z. Su, Y. Li, Q. Wu, D.X. Yang, Y.F. Chen, Shifeng Wang, NiP2/FeP heterostructural nanoflowers interwoven by carbon nanotubes as highly efficient electrocatalyst for oxygen evolution reaction, *J. Mater. Sci.* 56 (2021) 16000–16009, <https://doi.org/10.1007/s10853-021-06282-6>.

[35] Y.F. Liu, B. Wang, K. Srinivas, M.Y. Wang, Z. Chen, Z. Su, D.W. Liu, Y. Li, S. F. Wang, Y.F. Chen, CNT-interconnected iron-doped NiP2/NiP2 heterostructural nanoflowers as high-efficiency electrocatalyst for oxygen evolution reaction, *Int. J. Hydrog. Energ.* 47 (2022) 12903–12913, <https://doi.org/10.1016/j.ijhydene.2022.02.040>.

[36] K.N. Dinh, Q. Liang, C.-F. Du, J. Zhao, A.I.Y. Tok, H. Mao, Q. Yan, Nanostructured metallic transition metal carbides, nitrides, phosphides, and borides for energy storage and conversion, *Nano Today* 25 (2019) 99–121, <https://doi.org/10.1016/j.nantod.2019.02.008>.

[37] P.E.R. Blanchard, A.P. Grosvenor, R.G. Cavell, A. Mar, X-ray photoelectron and absorption spectroscopy of metal-rich phosphides M<sub>2</sub>P and M<sub>3</sub>P (M = Cr–Ni), *Chem. Mater.* 20 (2008) 7081–7088, <https://doi.org/10.1021/cm802123a>.

[38] P.W. Menezes, A. Indra, C. Das, C. Walter, C. Göbel, V. Gutkin, D. Schmeißer, M. Driess, Uncovering the nature of active species of nickel phosphide catalysts in high-performance electrochemical overall water splitting, *ACS Catal.* 7 (2016) 103–109, <https://doi.org/10.1021/acscatal.6b02666>.

[39] N. Thakur, M. Kumar, D. Mandal, T.C. Nagaiah, Nickel iron phosphide/phosphate as an oxygen bifunctional electrocatalyst for high-power-density rechargeable Zn–Air batteries, *ACS Appl. Mater. Interfaces* 13 (2021) 52487–52497, <https://doi.org/10.1021/acsami.1c12053>.

[40] J. Kupka, A. Budniok, Electrolytic oxygen evolution on Ni–Co–P alloys, *J. Appl. Electrochem.* 20 (1990) 1015–1020, <https://doi.org/10.1007/BF01019582>.

[41] A. Parra-Puerto, K.L. Ng, K. Fahy, A.E. Goode, M.P. Ryan, A. Kucernak, Supported transition metal phosphides: activity survey for HER, ORR, OER, and corrosion resistance in acid and alkaline electrolytes, *ACS Catal.* 9 (2019) 11515–11529, <https://doi.org/10.1149/MA2020-02372392mtgabs>.

[42] D. Huo, F. Song, J. Hu, J. Yuan, L. Niu, A.-J. Wang, One-step synthesis of carbon-encapsulated nickel phosphide nanoparticles with efficient bifunctional catalysis on oxygen evolution and reduction, *Int. J. Hydrog. Energy* 46 (2021) 8519–8530, <https://doi.org/10.1016/j.ijhydene.2020.12.050>.

[43] C.G. Read, J.F. Callejas, C.F. Holder, R.E. Schaaf, General strategy for the synthesis of transition metal phosphide films for electrocatalytic hydrogen and oxygen evolution, *ACS Appl. Mater. Interfaces* 8 (2016) 12798–12803, <https://doi.org/10.1021/acsami.6b02352>.

[44] R. Subbaraman, D. Tripkovic, K.C. Chang, D. Strmcnik, A.P. Paulikas, P. Hirunsit, M. Chan, J. Greeley, V. Stamenkovic, N.M. Markovic, Trends in activity for the water electrolyser reactions on 3d M(Ni,Co,Fe,Mn) hydr(oxy)oxide catalysts, *Nat. Mater.* 11 (2012) 550–557, <https://doi.org/10.1038/nmat3313>.

[45] A. Dutta, N. Pradhan, Developments of metal phosphides as efficient OER precatalysts, *J. Phys. Chem. Lett.* 8 (2017) 144–152, <https://doi.org/10.1021/acs.jpclett.6b02249>.

[46] Y. Wang, M. Wu, J. Li, H. Huang, J. Qiao, In situ growth of CoP nanoparticles anchored on (N,P) co-doped porous carbon engineered by MOFs as advanced bifunctional oxygen catalyst for rechargeable Zn–air battery, *J. Mater. Chem. A* 8 (2020) 19043–19049, <https://doi.org/10.1039/D0TA06435A>.

[47] M. Xiao, J. Zhu, L. Ma, Z. Jin, J. Ge, X. Deng, Y. Hou, Q. He, J. Li, Q. Jia, S. Mukerjee, R. Yang, Z. Jiang, D. Su, C. Liu, W. Xing, Microporous framework induced synthesis of single-atom dispersed Fe–N–C acidic ORR catalyst and its in situ reduced Fe–N<sub>4</sub> active site identification revealed by X-ray absorption spectroscopy, *ACS Catal.* 8 (2018) 2824–2832, <https://doi.org/10.1021/acs.catal.8b00138>.

[48] W. Chen, J. Pei, C.T. He, J. Wan, H. Ren, Y. Zhu, Y. Wang, J. Dong, S. Tian, W. C. Cheong, S. Lu, L. Zheng, X. Zheng, W. Yan, Z. Zhuang, C. Chen, Q. Peng, D. Wang, Y. Li, Rational design of single molybdenum atoms anchored on N-doped carbon for effective hydrogen evolution reaction, *Angew. Chem. Int. Ed. Engl.* 56 (2017) 16086–16090, <https://doi.org/10.1002/anie.201710599>.

[49] Z.H. Sheng, L. Shao, J.J. Chen, W.J. Bao, F.B. Wang, X.H. Xia, Catalyst-free synthesis of nitrogen-doped graphene via thermal annealing graphite oxide with melamine and its excellent electrocatalysis, *ACS Nano* 5 (2011) 4350–4358, <https://doi.org/10.1021/nn103584t>.

[50] H.B. Yang, J. Miao, S. Hung, J. Chen, H.B. Tao, X. Wang, L. Zhang, R. Chen, J. Gao, H.M. Chen, Identification of catalytic sites for oxygen reduction and oxygen evolution in N-doped graphene materials: Development of highly efficient metal-free bifunctional electrocatalyst, *Sci. Adv.* 2 (2016) 1501122, <https://doi.org/10.1126/sciadv.1501122>.

[51] Z.-F. Huang, J. Wang, Y. Peng, C.-Y. Jung, A. Fisher, X. Wang, Design of efficient bifunctional oxygen reduction/evolution electrocatalyst: recent advances and perspectives, *Adv. Energy Mater.* 7 (2017) 1700544, <https://doi.org/10.1002/aenm.201700544>.

[52] L.-Y. Jiang, X.-Y. Huang, A.-J. Wang, X.-S. Li, J. Yuan, J.-J. Feng, Facile solvothermal synthesis of Pt<sub>76</sub>Co<sub>24</sub> nanomyriapods for efficient electrocatalysis, *J. Mater. Chem. A* 5 (2017) 10554–10560, [https://doi.org/10.1039/C7TA01976A.](https://doi.org/10.1039/C7TA01976A)

[53] L. Peng, Y. Wang, I. Masood, B. Zhou, Y. Wang, J. Lin, J. Qiao, F.-Y. Zhang, Self-growing Cu/Sn bimetallic electrocatalysts on nitrogen-doped porous carbon cloth with 3D-hierarchical honeycomb structure for highly active carbon dioxide reduction, *Appl. Catal. B Environ.* 264 (2020), 118447, <https://doi.org/10.1016/j.apcatb.2019.118447>.

[54] K. Gong, F. Du, Z. Xia, M.F. Durstock, L. Dai, Nitrogen-doped carbon nanotube arrays with high electrocatalytic activity for oxygen reduction, *Science* 323 (2009) 760–764, <https://doi.org/10.1126/science.1168049>.

[55] J. Duan, S. Chen, M. Jaroniec, S. Qiao, Heteroatom-doped graphene-based materials for energy-relevant electrocatalytic processes, *ACS Catal.* 5 (2015) 5207–5234, <https://doi.org/10.1021/acscatal.5b00991>.

[56] Q. Wang, Y. Lei, Y. Zhu, H. Wang, J. Feng, G. Ma, Y. Wang, Y. Li, B. Nan, Q. Feng, Z. Lu, H. Yu, Edge defect engineering of nitrogen-doped carbon for oxygen electrocatalysts in Zn–air batteries, *ACS Appl. Mater. Inter.* 10 (2018) 29448–29456, <https://doi.org/10.1021/acsami.8b07863>.

[57] D.S. Yang, D. Bhattacharjya, S. Inamdar, J. Park, J.S. Yu, Phosphorus-doped ordered mesoporous carbons with different lengths as efficient metal-free electrocatalysts for oxygen reduction reaction in alkaline media, *J. Am. Chem. Soc.* 134 (2012) 16127–16130, <https://doi.org/10.1021/ja306376s>.